Pre-synaptic DC bias controls the plasticity and dynamics of three-terminal neuromorphic electrolyte-gated organic transistors

NEUROMORPHIC
Computing and Engineering

OPEN ACCESS

RECEIVED
21 October 2022

REVISED
3 January 2023

ACCEPTED FOR PUBLICATION
16 January 2023

PUBLISHED
31 January 2023

PAPER

Pre-synaptic DC bias controls the plasticity and dynamics of three-terminal neuromorphic electrolyte-gated organic transistors

Federico Rondelli[1,2], Anna De Salvo[1,2], Gioacchino Calandra Sebastianella[1,3], Mauro Murgia[1,4], Luciano Fadiga[1,2], Fabio Biscarini[1,5] and Michele Di Lauro[1,*]

[1] Center for Translational Neurophysiology of Speech and Communication, Fondazione Istituto Italiano di Tecnologia (IIT-CTNSC), via Fossato di Mortara 17/19, Ferrara 44121, Italy
[2] Sezione di Fisiologia Dipartimento di Neuroscienze e Riabilitazione, Università di Ferrara, via Fossato di Mortara 17/19, Ferrara 44121, Italy
[3] Dipartimento di Scienze Biomediche, Metaboliche e Neuroscienze,Università di Modena e Reggio Emilia, 41125 Modena, Italy
[4] Istituto per lo Studio dei Materiali Nanostrutturati (CNR-ISMN), National Research Council, via Gobetti 101, Bologna 40129, Italy
[5] Dipartimento di Scienze della Vita Università di Modena e Reggio Emilia, Via Campi 103, Modena 41125, Italy
[*] Author to whom any correspondence should be addressed.

E-mail: michele.dilauro@iit.it

Keywords: organic neuromorphic electronics, electrolyte-gated organic transistor, paired-pulse plasticity, PEDOT:PSS

Abstract

The role of pre-synaptic DC bias is investigated in three-terminal organic neuromorphic architectures based on electrolyte-gated organic transistors—EGOTs. By means of pre-synaptic offset it is possible to finely control the number of discrete conductance states in short-term plasticity experiments, to obtain, at will, both depressive and facilitating response in the same neuromorphic device and to set the ratio between two subsequent pulses in paired-pulse experiments. The charge dynamics leading to these important features are discussed in relationship with macroscopic device figures of merit such as conductivity and transconductance, establishing a novel key enabling parameter in devising the operation of neuromorphic organic electronics.

1. Introduction

The recent effort towards the development of efficient neuromorphic components and devices, aimed at coupling high computational efficiency with low power consumption by mutating processing and learning paradigms for neural systems, led to identify a number of candidate materials and device architectures [1]. Organic (semi-)conductive materials possess highly desirable figures of merit for devising neuromorphic organic electronic systems. Neuromorphic properties, such as spike time dependent plasticity [2], control on global connectivity [3], multiterminal operations [4] and time-dependent pattern classification [5] were demonstrated with organic device architectures. Organic neuromorphic devices are often termed organic artificial synapses in analogy with neural synapses.

The neuromorphic response of organic electronic devices arises by the dynamics following the out-of-equilibrium displacement (by means of an input signal) of the active material (the organic (semi-)conductor) initially at equilibrium with the operational electrolyte [6]. Since the equilibrium involves all the species dissolved in the solution, the artificial synapses will respond differently to different compositions of the solution. In the presence of strong interactions between some solute species and the material, the dynamics of recovery the equilibrium condition, once the input signal is removed, can be particularly slow. Artificial synapse architectures effectively sense those moieties in solution that give rise to strong, albeit not necessarily specific, interactions. Indeed, administration of square voltage pulses at a fixed frequency (as input signal) results for the species with strong interactions in the kinetic unbalance between the processes of adsorption/retention and desorption/expulsion in/out the organic active material [7, 8]. Each input voltage pulse drives the organic (semi) conductor to a 'metastable' state with a different conductance level with respect to the initial one (the baseline). The response to the sequence of input voltage pulses is a ladder of current spikes of different intensities, either decreasing (depressive short-term

plasticity—STP—response) or increasing (facilitating STP response). Once in the final metastable state, the conductance/current relaxes to the initial baseline value with a time scale characteristic of the composition of the solution, of the baseline and of the features (amplitude, frequency and number of spikes) of the input signal. This means that the initial and final conductance states of artificial synapses in response to a defined input signal are connected through a precise pathway. One can also regard the relaxation time from the final metastable state to the initial state as the result of training the device by means of the input signal, because the relaxation is characteristic of the two states connected by the input signal. If the relaxation time is long, then the artificial synapse has kept memory of the input signal, and in case of very long time scales we term this long-term plasticity—LTP.

It is clear that the behavior of artificial synapse arises from the interplay between active material conductance and ion density in close proximity to the material itself, resulting in the newly coniated definition of such materials as organic mixed ionic-electronic conductors—OMIECs [9].

If this is true in the steady-state, it becomes even more critical when dealing with transient phenomena, in which the dramatic difference between ion dynamics and charge transport dynamics gives rise to a complex out-of-equilibrium behavior, which is regarded as the origin of the neuromorphic response.

The key role of the Gibbs free energy in determining kinetics and magnitude of doping/dedoping processes in OMIECs, and, in particular, in the most widespread poly(3,4-ethylenedioxythiophene): polystyrene sulfonate—PEDOT:PSS—has been demonstrated and exploited in the development of binding-energy-specific sensors [6]. Lately, it was unambiguously demonstrated how OMIEC conductance is a cumulative observable which provides a comprehensive insight on the thermodynamic and kinetic condition of the electrolyte/OMIEC system [10]. Interestingly, such phenomena can be observed also in non-OMIEC-based architectures, provided that they integrate ionic density in proximity with a (semi-)conductive channel in their working principle (e.g. using poly-electrolytes as dielectric layers) [11, 12].

Among organic electronic device architectures, the one which majorly benefits from the above discussed features and integrates them in its functional principle is the electrolyte-gated organic transistor—EGOT [13]. In EGOTs, a semi-conductive film bridges two contacts—termed source (S) and drain (D)—and it is directly exposed to an electrolyte, whose potential is set by a third contact—termed gate (G)—directly bathing in the electrolyte. In such architectures, small gate voltage—V_{GS}—variations result in significant channel current—I_{DS}—variations, making EGOTs ideal platforms for transduction [14–16] and sensing applications [17–19]. A quantitative figure of merit for such applications of EGOT technology is the transconductance, $g_m = dI_{DS}/dV_{GS}$.

Focusing on different aspects of their working principle, EGOTs are referred to as electrolyte-gated organic field-effect transistors—EGOFETs [20], organic electro-chemical transistors—OECTs [21] or ion-gated transistors—IGT [22]. The key aspect of all these architectures is the role of the gate electrode in setting the organic semiconductor conductance. As discussed above, this implies a direct role of the gate electrode on the Gibbs free-energy of the system and, subsequently, on its response kinetics when it is operated as an artificial synapse. According to this and to some previous observations in similar architectures [23], the hypothesis addressed in this work is that a modulation of the DC offset at the gate electrode—usually termed pre-synaptic terminal in neuromorphic architectures—should imply not only a modulation of steady-state observables such as channel (trans-)conductance but also a difference in transient aspects, such as the temporal evolution of the 'post-synaptic' channel current.

In this work, the hypothesis is tested against standard neuromorphic characterization protocols and rationalized in terms of displaced charge. We highlight the key role of transconductance as an estimator for amplitude, resolution, time evolution and 'direction' of xeromorphic phenomena in artificial synapses based on EGOT architectures. This work provides a comprehensive discussion on the use of pre-synaptic DC offset at the gate electrode, which governs trans conductance, as a prompt tuning tool towards the response of such devices, achieving fine modulation of transient STP and LTP effects in the post-synaptic drain-source current, reversibly switching from depressing to potentiating behavior, without the need of changing active material [24, 25], of permanently altering the device layout [26] or of rearranging the connection layout [23].

2. Results and discussion

PEDOT:PSS-based EGOTs were fabricated as described in the Experimental section and their steady-state *I–V* response has been characterized. Results are summarized in figure 1. Figure 1(a) schematically shows the chosen EGOT architecture with the common-source/common-ground connection layout. Figure 1(b) reports a representative transfer characteristic (forward and backward gate sweep), I_{DS} vs V_{GS}, and the corresponding transconductance (estimated as first derivative from the forward scan branch), g_m vs V_{GS}. The plot also evidences a negligible leakage I_{GS} current, a modest clockwise hysteresis and a maximum

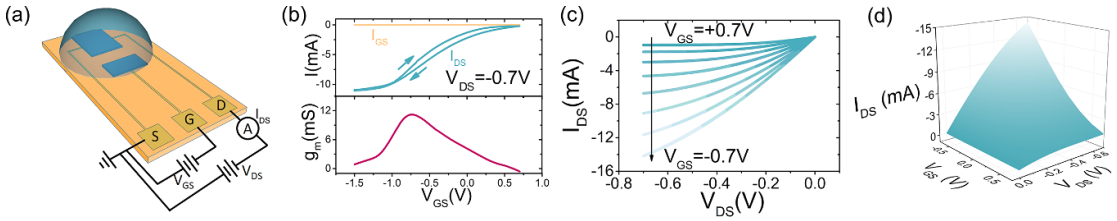

Figure 1. (a) Schematic 3D representation of the proposed EGOT with patterned PEDOT:PSS channel and gate, contacted by gold leads, operated in common-source/common-ground configuration; (b) representative transfer characteristic of the proposed neuromorphic EGOT, reporting channel current—I_{DS} (blue solid line), leakage current—I_{GS} (orange solid line) and transconductance—g_m (magenta solid line) as a function of V_{GS}; (c) representative output characteristics for $-0.7\ \text{V} < V_{DS} < 0\ \text{V}$ and $-0.7\ \text{V} < V_{GS} < 0.7\ \text{V}$; (d) 3D plots showing the dependence of I_{DS} from both V_{GS} and V_{DS}.

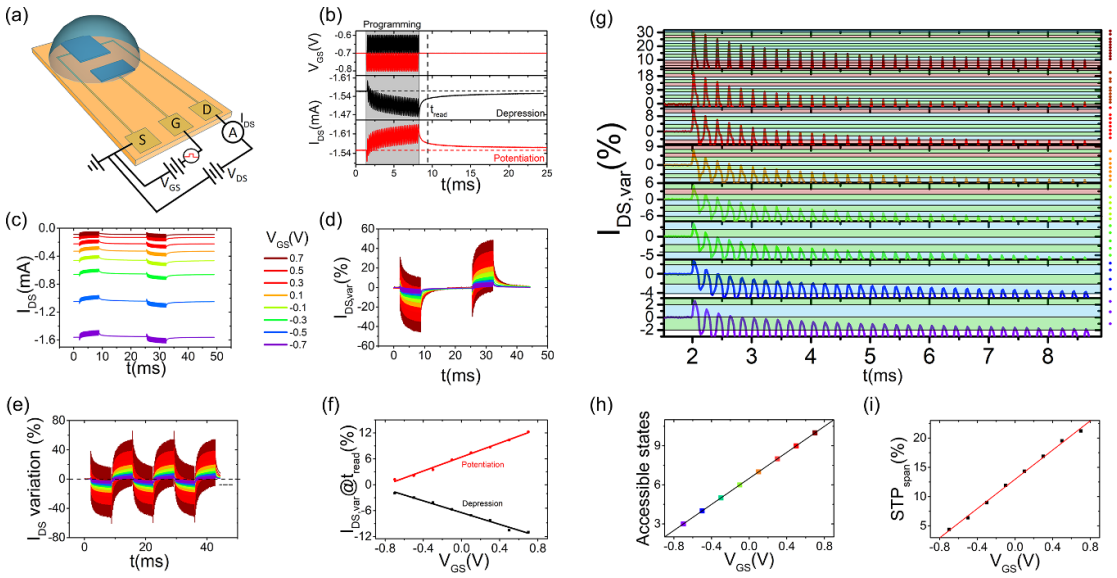

Figure 2. (a) Connection layout for the neuromorphic EGOT. Gate terminal is the pre-synaptic electrode with applied square pulses and controlled DC offset, I_{DS} is the post-synaptic current flowing between Source and Drain terminals. The driving voltage ($V_{DS} = -0.7$ V) is kept constant; (b) voltammograms of EGOT training for achieving potentiating (red solid line) and depressive (black solid line) short-term plasticity and relative current responses. The reading time to assess plasticity—t_{read}—is highlighted; (c) current responses to two subsequent programming/reading cycles (first depressive, then potentiating) at various V_{GS} DC offsets; (d) relative post-synaptic current variations with respect to baseline, at various V_{GS} DC offsets; (e) relative post-synaptic current variations at $t = t_{read}$ vs V_{GS} DC offset, in response to potentiating (red dots) and depressive (black dots) programming, with linear fits; (f) continuous switching between potentiation and depression upon voltage trains of opposite sign; (g) zoom on the maxima of $I_{DS,var}$ vs t in a depressive programming cycle at various V_{GS} DC biases, highlighting discrete conductivity states accessed during programming (discretization threshold $\Delta I_{DS,var} = 2\%$—green and light blue windows) and inaccessible states (red windows); (h) linear dependency of STP_{span} on V_{GS}; (i) linear dependency of the number of accessible discrete conductance states on V_{GS}.

$g_m \approx 12$ mS at $V_{GS} \approx -0.75$ V. Output characteristics (figure 1(c)) show ohmic behavior at $V_{DS} \leqslant 0$ with gate dependent saturation plateaus, as expected for p-type depletion mode EGOTs. These EGOTs are in line with the state-of-the-art PEDOT:PSS-based devices and exhibit the well-known dependence of I_{DS} on V_{GS} and on V_{DS}, as evidenced by the 3D plot in figure 1(d).

The role of DC pre-synaptic bias in governing the neuromorphic response of EGOTs was investigated by characterizing the short-term plasticity (STP) response of the post-synaptic current—I_{DS}—to square voltage pulses superimposed to the DC offset at the pre-synaptic terminal (i.e. the gate electrode). In figure 2(a) the schematic drawing of the device layout with the connections evidences the input voltage generator connected to the gate, and the amperometer to the drain electrode. A representative STP characterization is shown in figure 2(b): upon a train of voltage square pulses, either positive or negative, termed programming phase, the response of neuromorphic EGOTs is either depressed or potentiated. These responses are due to the progressive accumulation (in the case of depression) or depletion (in the case of potentiation) of cations in close proximity of the PEDOT:PSS channel upon repeated pulsing. Upon each pulse, the device responds with an I_{DS} current spike that partially relaxes before the next voltage pulse is administered. The result is the mean I_{DS} current (and its conductance) drifting towards a novel, dynamical steady state different from the

initial equilibrium state. When the programming phase is over, the channel current/conductance slowly relaxes back to its initial DC value.

Figure 2(c) shows the I_{DS} response to two subsequent (first depressive, then potentiating) STP programming cycles. The current baseline moves towards lower conductance steady states for V_{GS} increasing from −0.7 V to 0.7 V. This modulation of the baseline conductance value by the pre-synaptic DC bias is indeed expected from EGOT I–V characteristics (figure 1). Surprisingly, instead, the transient current response to the pre-synaptic DC bias exhibits much larger relative variation as the V_{GS} becomes more positive. This can be evidenced by expressing the STP response in terms of percentage current variation with respect to the baseline.

$$I_{DS}, \mathrm{var} = 100 \times \frac{I_{DS}(t) - I_{DS}(0)}{I_{DS}(0)}.$$

Figure 2(d) shows that more positive V_{GS} values (lower PEDOT:PSS baseline conductance) yield greater $I_{DS,var}$ for both programming and relaxation phases. Importantly, these effects of pre-synaptic DC bias are conserved also upon repeated reversible switching between depressive and potentiating STP programming phases (figure 2(e)).

Moreover, as evidenced in figure 2(f), the relaxation kinetics is also slower. This is inferred by setting an arbitrary reading time, t_{read} (vertical dashed line in figure 2(b)), after the programming phase end, and measuring the relative increase/decrease of the current from the minimum/maximum of the last programming pulse. Figure 2(f) shows the linear correlation between the DC V_{GS} bias and the residual $I_{DS,var}$ at t_{read}, for both potentiation and depression. The combined effects of modulated relative amplitude and relaxation time scale open unprecedented possibilities for the use of such devices in neuromorphic circuitry. Indeed, by setting the DC pre-synaptic bias, it is possible to decide if a certain programming phase results in the storage of information and also the relative magnitude of the stored information. An additional critical parameter which is directly controlled by the DC V_{GS} bias is the number of discrete accessible conductance states during programming (figure 2(g)). In detail, by setting a discretization threshold of $\Delta I_{DS,var} = 2\%$ to discriminate between two states, it is evident that the higher the $I_{DS,var}$ (i.e. the more positive the V_{GS}), the larger the number of conductance states. Figure 2(g) shows a zoom on the $I_{DS,var}$ maxima during a depressive STP programming cycle, V_{GS} values spanning from −0.7 V to 0.7 V. Conductance states are identified by horizontal lines at multiples of 2% $I_{DS,var}$, accessible states (i.e. states in which maxima actually fall) are highlighted in green and blue and counted by dots on the right axis, prohibited states are highlighted in red. As shown in figure 2(h), also the number of accessible states scales linearly with V_{GS} and goes from 3 to 10 while moving from negative V_{GS} values to positive ones.

A useful tool to provide an *a priori* estimate of the number of accessible conductance states, n, for a given discretization threshold, d_{th}, which shall be set according to the resolution of the readout strategy in the desired neuromorphic application, can be given in terms of STP_{span}, defined as the absolute value of the difference between $I_{DS,var}$ in response to the first programming pulse and $I_{DS,var}$ in response to the last one. In particular,

$$n = \mathrm{int}\left(STP_{span}/d_{th}\right) + 1.$$

As a consequence, in the proposed neuromorphic EGOTs, the linear relation between STP_{span} and V_{GS} is mirrored by a linear n vs V_{GS} dependence in the considered V_{GS} range (figure 2(i)).

Such profound effect of DC gate voltage on neuromorphic phenomena can be rationalized in terms of exchanged charge upon programming. As a consequence, it is necessary to extensively characterize the channel response upon the application of square pulses (figures 3(a) and (b)). A single square voltage pulse—either positive or negative (top panels)—is applied at the pre-synaptic electrode while measuring the elicited current in the post-synaptic channel between the source and drain electrode (center panels). The measured post-synaptic I_{DS} is then integrated in time to obtain chronocoulograms (Q vs t), here reported in terms of charge variation (ΔQ) with respect to the charge value before pulse administration (bottom panels). This protocol is repeated for various DC $V_{GS,Offset}$ values, ranging from −0.7 V to 0.7 V, resulting in the trends depicted in figures 3(c) and (d).

Concerning the single negative pulse, figure 3(c), it is possible to observe how during the pulse there is a linear time profile of ΔQ, whose slope (i.e. magnitude for constant pulse duration) depends on the applied $V_{GS,Offset}$. A phenomenologically consistent behavior can be observed in response to positive single pulses, albeit with an opposite sign and different magnitude (figure 3(d)). Figures 3(e) and (f) show the magnitude of the exchanged charge in the channel upon pulse administration as a function of $V_{GS,pulse}$ for negative and positive voltage pulses, respectively. Here $V_{GS,pulse}$ equals $V_{GS,Offset} - 0.5$ V for negative pulses and $V_{GS,Offset} + 0.5$ V for positive ones.

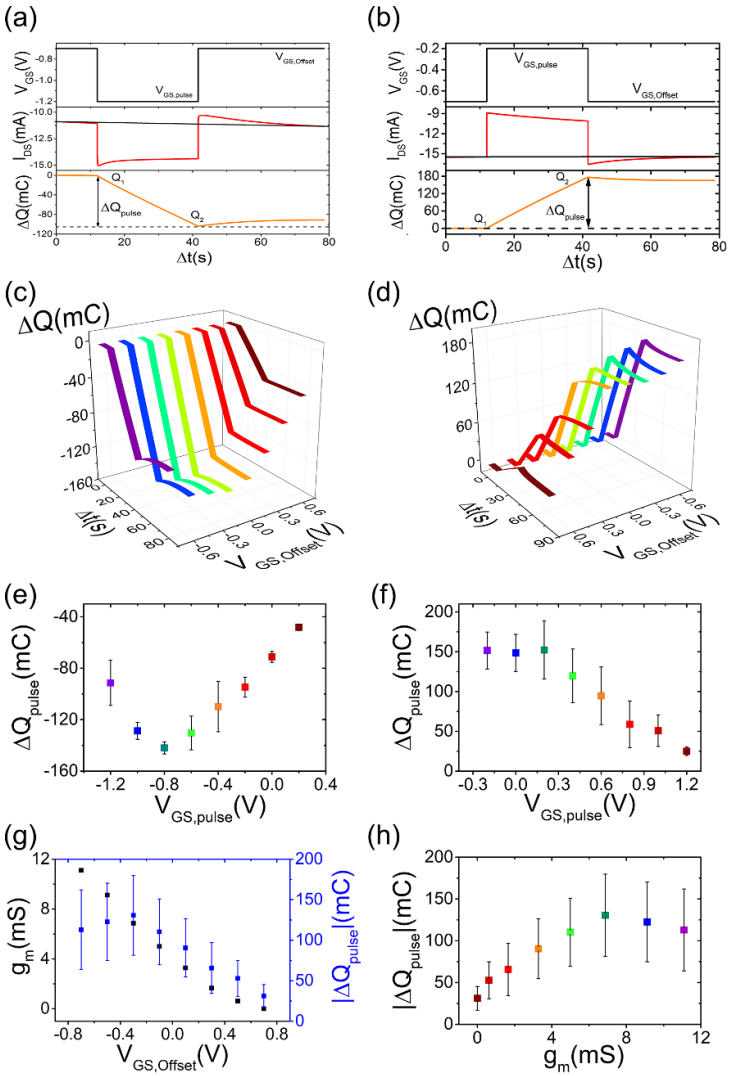

Figure 3. (a)–(b) Cronovoltammogram (black solid line) applied at the pre-synaptic electrode, Cronoamperogram (red solid line) measured at the post-synaptic channel and Cronoculogram (orange solid line) of single negative (a) or positive (b) square pulse; (c)–(d) 3D-plot of the exchanged ΔQ during the negative (c) or positive (d) square pulse protocol highlighting the ΔQ dependencies on time and DC $V_{GS,Offset}$; (e)–(f) exchanged channel charge during the negative (e) and positive (f) pulse at different $V_{GS,pulse}$ ($n = 4$, standard deviations as error bars); (g) transconductance and absolute value of the average ΔQ_{pulse} ($n = 4$, propagated standard deviations as error bars) vs $V_{GS,Offset}$; (h) correlation plot of $|\Delta Q_{pulse}|$ with the channel transconductance.

The non-linear trends in figures 3(e) and (f) can be rationalized assuming that the charge exchanged in the channel during the single pulse is affected by the channel doping prior to the pulse administration and by its proneness to be altered which is physically measured by the transconductance. Indeed, both are set by $V_{GS,Offset}$. A demonstration is given in figure 3(g), which shows the overlay between the trends of the transconductance, g_m, and of the absolute value of charge exchanged in the channel during pulse administration, $|\Delta Q_{pulse}|$, vs $V_{GS,Offset}$. It is possible to observe a clear correlation between these two observables (figure 3(h)), especially at small transconductance (else positive $V_{GS,Offset}$ values), which is progressively lost upon moving towards fully doped channels (at strongly negative $V_{GS,Offset}$). The charge variation saturates when transconductance attains its highest values.

Noticeably, as reported in figures 3(c) and (d), upon pulse removal, ΔQ does not always remain constant. Yet, it may exhibit different relaxation kinetics, which vary according to the $V_{GS,Offset}$ and, hence, to g_m, before reaching a steady-state value. In particular, for high transconductances, the system exhibits an overcharging—or an overdepletion for positive pulses—upon pulse administration, which needs to be recovered in time, following the kinetics of the relevant displaced charged species (i.e. anions or cations) in the electrolyte at the interface with the channel. On the other hand, in regimes of low transconductance, pulse removal results in total cessation of charge exchange in the channel in the case of negative pulses, whereas it causes slow charge accumulation in the case of positive ones. This important difference can be ascribed to the different sign and hidro-dynamic volume of the ions which come into play, according to the

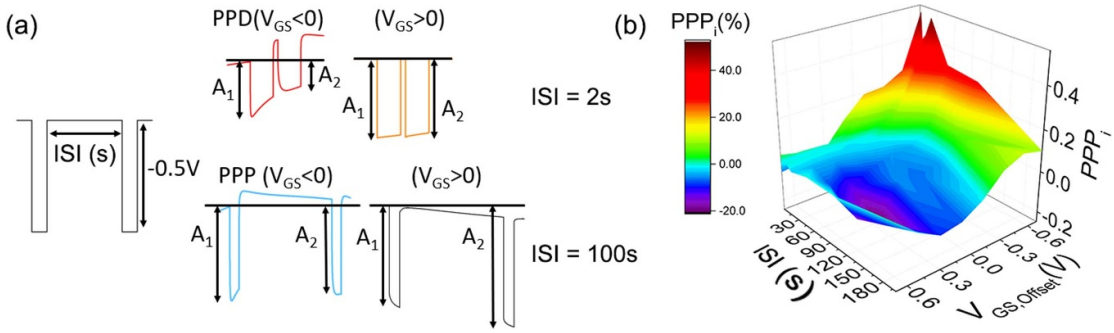

Figure 4. (a) Schematic representation of pre-synaptic voltage paired pulses (on the left) and measured post-synaptic currents (on the right) highlighting the depressive and facilitative behavior induced by the application of $V_{GS,Offset}$ at the presynaptic terminal, for different ISI durations; (b) 3D surface that correlates the applied DC $V_{GS,Offset}$ with the ISI in seconds and an averaged paired pulse plasticity index (PPP_i, $n = 4$) to quantify plasticity phenomena.

pulse sign, coupled to the 'accessible' coordination sites for ions present in the channel, set by $V_{GS,Offset}$. In this sense, this kinetic processes closely mirror the behavior of transconductance and, for this reason, transconductance non-linearity is at the origin of neuromorphic tunability in EGOTs.

The applicability of such concepts to neuromorphic circuitry development is assessed in a paired-pulse experiment, investigating depressive and facilitating phenomena upon the application of paired square pulses (amplitude −500 mV) at the pre-synaptic gate terminal, while varying the inter-stimulation interval—ISI—from 20 ms up to 200s and $V_{GS,offset}$ from −0.7 V to 0.7 V (figure 4(a), left). A quantitative representation of the entity of depression/facilitation can be given defining a paired-pulse plasticity index—PPP_i:

$$\mathrm{PPP}_i = 1 - \frac{A_2}{A_1}.$$

In such definition, A_1 and A_2 are the differences between post-synaptic current peaks (in response to the first and the second pre-synaptic pulse, respectively) and the baseline current value before pulse administration, as shown in representative traces in figure 4(a). Positive values of PPP_i indicate a depressive response while negative values testify a facilitative behavior; in both cases, $|PPP_i|$ measures the entity of the phenomenon.

PPP_i dependency on $V_{GS,offset}$ and ISI is shown in figure 4(b). It is possible to distinguish between four main scenarios:

(a) When ISI is short and the semiconductive channel is ON (i.e. at negative $V_{GS,offset}$ values), a depressive response is observed, with $PPP_i > 0$. This is the most commonly reported case in the literature;
(b) When ISI is short and the semiconductive channel is OFF (i.e. at positive $V_{GS,offset}$ values), the system responds linearly with $PPP_i \approx 0$;
(c) When ISI is long and the channel is ON, the system exhibits depressive response, although of smaller magnitude (i.e. smaller positive PPP_i values);
(d) When ISI is long and the channel is OFF, it is possible to achieve consistent potentiation of the post-synaptic current (i.e. $PPP_i < 0$).

Noticeably, a number of intermediate situations can be obtained while moving in between these four extremes, resulting in the possibility of arbitrarily selecting PPP_i by properly tuning ISI and $V_{GS,offset}$.

It is important to highlight the fact that, at the origin of scenarios 3 and 4, there is the same physical peculiarity of the channel. In particular, if the channel is left unperturbed for a certain amount of time and, at the same time, it is exposed to a constant $V_{GS,offset}$ value, its conductivity tends to increase. This is surprising since constant $V_{GS,offset}$ should imply a constant ionic environment in close proximity to the channel which should set a single conductivity value in EGOTs. The fact that this effect is more pronounced in the case of positive $V_{GS,offset}$, when cations are forced at the interface with the PEDOT:PSS channel, hints at the presence of slow rearrangement phenomena which allow the system to 'cope' to the presence of cations and to partially restore, in time, its conductivity. This explanation, which ultimately implies the presence of kinetically stored electrostatic energy in PEDOT:PSS films at the interface with electrolytes, is in good agreement with previous reports of the existence of electrochemical pseudo-inductive contributions to such

interfaces [7], which give rise to facilitative plasticity responses at long ISI and widens the applicability context of neuromorphic EGOTs.

3. Experimental

3.1. EGOT fabrication

Custom test patterns were designed and purchased by Phoenix PCB (Ivrea, Italy). The final design features nine independent pairs of gold source/drain electrodes ($W = 400$ μm, $L = 100$ μm, $W/L = 4$) patterned onto a flexible poly-imide substrate. Insulation is guaranteed by an additional polyimide layer with nine passing holes, which covers the entire layout and exposes only the terminal portion (area $= 0.8 \times 0.9$ mm) of the electrode leads. Semi-conductive channels and gate electrodes are obtained filling the nine pools with 500 nL of a PEDOT:PSS formulation (Clevios PH1000, 5% v/v DMSO, 0.2% v/v GOPS; diluted 10 times with Milli-Q water) and curing in a thermostatic oven (120 °C, 30 min). Obtained films exhibit an average 1 μm thickness (XE7 AFM Park System, tapping mode). Stability and repeatability of the steady state operations of such EGOT arrays were previously reported elsewhere [23].

3.2. Electrical characterization

Steady-state electrical characterization is performed using a two-channel Keysight B2912A Source/Measure Unit, equipped with two Keysight N1294A Opt001 banana-triax adapters, in common-source/common-ground configuration. The characterization layout is achieved by connecting the Source electrode to the short-circuited 'low' terminals of the two channels, while connecting the Gate and the Drain electrodes to the 'high' terminals of channel 1 and channel 2, respectively. Measurements are performed using 1 M phosphate buffered saline solution at pH = 7.4 (P3619-1 GA, Merck) as an electrolyte. *I–V* transfer characteristics are acquired sweeping V_{GS} from −1.2 V to 0.7 V (scan rate = 950 mV s^{-1}), while keeping fixed $V_{DS} = -0.7$ V.

I–V output characteristics are acquired by cycling V_{DS} from 0.0 V to −0.7 V, changing the fixed V_{GS} value at each cycle from −0.7 V to 0.7 V with steps of 0.2 V.

Neuromorphic response is investigated in the very same layout as steady-state *I–V* performance, by adding a programming step of the AC pre-synaptic V_{GS} voltage by means of a custom designed software, acquiring the post-synaptic current I_{DS} vs time and varying the V_{GS} DC-offset ranging from −0.7 V to 0.7 V with steps of 0.2 V. In particular:

(a) short-term plasticity is characterized with trains of 5 kHz V_{GS} square pulses, featuring an absolute amplitude of 10 mV, inverting pulse sign each 34 pulses;
(b) responses to single pulses are investigated by administering V_{GS} square pulses (amplitude $= -0.5$ V, duration = 20 s);
(c) paired-pulse plasticity is assessed with 2 subsequent V_{GS} square pulses (amplitude $= -0.5$ V, duration = 10 s), varying the inter-pulse interval from 20 ms to 200s.

3.3. Analysis, graphing and presentation

Collected data are analyzed and graphed by means of OriginPro2016, figure panels are assembled in Adobe Photoshop CS6, 3D-device schematics are sketched in SketchUp Make 2017.

4. Conclusions

In this work, a comprehensive study on the critical importance of the DC offset bias at the gate electrode in determining the neuromorphic response of EGOTs is presented. $V_{GS,offset}$ is shown to control the number of accessible discrete conductance states in short-term plasticity-based memories, operated both in depression and in potentiation. It is discussed the relationship between $V_{GS,offset}$, device transconductance and exchanged charge upon pulse administration and it is explained how the complex interplay between these parameters governs neuromorphism. Finally, paired-pulse plasticity is investigated as a function of $V_{GS,offset}$, leading to a tuning map for PPP_i in EGOT-based neuromorphic applications.

These results add a degree of freedom in the design of neuromorphic circuitry by endowing the operator of an additional powerful tuning parameter, whose role arises from the peculiar features of EGOTs, paving the way towards the new-generation organic neuromorphic platform for real-time signal processing and pattern recognition.

Data availability statement

The data that support the findings of this study are available upon reasonable request from the authors.

Acknowledgments

Research work leading to this publication was funded by IIT—Istituto Italiano di Tecnologia, University of Ferrara and University of Modena and Reggio Emilia (FAR 2018 Project e-MAP).

ORCID iD

Michele Di Lauro https://orcid.org/0000-0002-7072-9468

References

[1] Christensen D V *et al* 2022 2022 roadmap on neuromorphic computing and engineering *Neuromorph. Comput. Eng.* **2** 022501
[2] Gkoupidenis P, Schaefer N, Garlan B and Malliaras G G 2015 Neuromorphic functions in PEDOT:PSS organic electrochemical transistors *Adv. Mater.* **27** 7176–80
[3] Gkoupidenis P, Koutsouras D A and Malliaras G G 2017 Neuromorphic device architectures with global connectivity through electrolyte gating *Nat. Commun.* **8** 1–8
[4] Koutsouras D A, Prodromakis T, Malliaras G G, Blom P W M and Gkoupidenis P 2019 Functional connectivity of organic neuromorphic devices by global voltage oscillations *Adv. Intell. Syst.* **1** 1900013
[5] Pecqueur S, Mastropasqua Talamo M, Guérin D, Blanchard P, Roncali J, Vuillaume D and Alibart F 2018 Neuromorphic time-dependent pattern classification with organic electrochemical transistor arrays *Adv. Electron. Mater.* **4** 1–9
[6] Giordani M, Sensi M, Berto M, Di Lauro M, Bortolotti C A, Gomes H L, Zoli M, Zerbetto F, Fadiga L and Biscarini F 2020 Neuromorphic organic devices that specifically discriminate dopamine from its metabolites by nonspecific interactions *Adv. Funct. Mater.* **30** 2002141
[7] Calandra Sebastianella G, Di Lauro M, Murgia M, Bianchi M, Carli S, Zoli M, Fadiga L and Biscarini F 2021 Implantable organic artificial synapses exhibiting crossover between depressive and facilitative plasticity response *Adv. Electron. Mater.* **2100755** 2100755
[8] Giordani M, Berto M, Di Lauro M, Bortolotti C A, Zoli M and Biscarini F 2017 Specific dopamine sensing based on short-term plasticity behavior of a whole organic artificial synapse *ACS Sensors* **2** 1756–60
[9] Paulsen B D, Tybrandt K, Stavrinidou E and Rivnay J 2020 Organic mixed ionic–electronic conductors *Nat. Mater.* **19** 13–26
[10] Rebetez G, Bardagot O, Affolter J, Réhault J and Banerji N 2022 What drives the kinetics and doping level in the electrochemical reactions of PEDOT:PSS? *Adv. Funct. Mater.* **32** 2105821
[11] Feng G *et al* 2020 A Sub-10 nm vertical organic/inorganic hybrid transistor for pain-perceptual and sensitization-regulated nociceptor emulation *Adv. Mater.* **32** 1906171
[12] Jiang J, Hu W, Xie D, Yang J, He J, Gao Y and Wan Q 2019 2D electric-double-layer phototransistor for photoelectronic and spatiotemporal hybrid neuromorphic integration *Nanoscale* **11** 1360–9
[13] Di Lauro M *et al* 2020 A bacterial photosynthetic enzymatic unit modulating organic transistors with light *Adv. Electron. Mater.* **6** 1900888
[14] Di Lauro M, Zucchini E, De Salvo A, Delfino E, Bianchi M, Murgia M, Carli S, Biscarini F and Fadiga L 2022 A novel biasing scheme of electrolyte-gated organic transistors for safe *in vivo* amplification of electrophysiological signals *Adv. Mater. Interfaces* **9** 2101798
[15] Cramer T, Campana A, Leonardi F, Casalini S, Kyndiah A, Murgia M and Biscarini F 2013 Water-gated organic field effect transistors–opportunities for biochemical sensing and extracellular signal transduction *J. Mater. Chem.* B **1** 3728–41
[16] Khodagholy D *et al* 2013 *In vivo* recordings of brain activity using organic transistors *Nat. Commun.* **4** 1575
[17] Seshadri P, Manoli K, Schneiderhan-Marra N, Anthes U, Wierzchowiec P, Bonrad K, Di Franco C and Torsi L 2018 Low-picomolar, label-free procalcitonin analytical detection with an electrolyte-gated organic field-effect transistor based electronic immunosensor *Biosens. Bioelectron.* **104** 113–9
[18] Berto M *et al* 2019 Label free detection of plant viruses with organic transistor biosensors *Sens. Actuators* B **281** 150–6
[19] Selvaraj M, Greco P, Sensi M, Saygin G D, Bellassai N, D'Agata R, Spoto G and Biscarini F 2021 Label free detection of miRNA-21 with electrolyte gated organic field effect transistors EGOFETs) *Biosens. Bioelectron.* **182** 113144
[20] Casalini S, Leonardi F, Cramer T and Biscarini F 2013 Organic field-effect transistor for label-free dopamine sensing *Org. Electron.* **14** 156–63
[21] Campana A, Cramer T, Simon D T, Berggren M and Biscarini F 2014 Electrocardiographic recording with conformable organic electrochemical transistor fabricated on resorbable bioscaffold *Adv. Mater.* **26** 3874–8
[22] Cea C, Spyropoulos G D, Jastrzebska-Perfect P, Ferrero J J, Gelinas J N and Khodagholy D 2020 Enhancement-mode ion-based transistor as a comprehensive interface and real-time processing unit for *in vivo* electrophysiology *Nat. Mater.* **19** 679–86
[23] Di Lauro M, De Salvo A, Sebastianella G C, Bianchi M, Carli S, Murgia M, Fadiga L and Biscarini F 2020 Tunable short-term plasticity response in three-terminal organic neuromorphic devices *ACS Appl. Electron. Mater.* **2** 1849–54
[24] Yamamoto S and Malliaras G G 2020 Controlling the neuromorphic behavior of organic electrochemical transistors by blending mixed and ion conductors *ACS Appl. Electron. Mater.* **2** 2224–8
[25] Di Lauro M, Berto M, Giordani M, Benaglia S, Schweicher G, Vuillaume D, Bortolotti C A, Geerts Y H and Biscarini F 2017 Liquid-gated organic electronic devices based on high-performance solution-processed molecular semiconductor *Adv. Electron. Mater.* **3** 1–6
[26] Gerasimov J Y, Gabrielsson R, Forchheimer R, Stavrinidou E, Simon D T, Berggren M and Fabiano S 2019 An evolvable organic electrochemical transistor for neuromorphic applications *Adv. Sci.* **6** 1–8